

Propagation of stationary planetary waves to the thermosphere at different levels of solar activity



A.V. Koval^{a,*}, N.M. Gavrilov^a, A.I. Pogoreltsev^{a,b}, N.O. Shevchuk^a

^a Saint-Petersburg State University, Department of Atmospheric Physics, 198504, St. Petersburg, Russia

^b Russian State Hydrometeorological University, Department of Meteorological Forecasts, Saint-Petersburg, Russia

ABSTRACT

Numerical modeling of changes in the global atmospheric circulation and characteristics of stationary planetary waves with zonal wavenumbers 1–4 is performed, taking into account the effects of changes in solar activity at altitudes above 100 km. The middle and upper atmosphere model (MUAM) is utilized to simulate the general circulation and planetary waves at altitudes 0–300 km, averaged over 12-member ensemble of model runs for values of the solar radio flux at the wavelength of 10.7 cm corresponding to the high and low levels of solar activity. The ionospheric conductivities and their latitudinal, longitude and temporal dependences are taken into account in the MUAM. Calculations for January–February in the thermosphere showed larger eastward wind velocity at altitudes above 130 km at high solar activity level. In the thermosphere, the amplitudes of planetary waves decrease at most latitudes at high solar activity level. Simulated changes in the atmospheric refractivity index and the Eliassen–Palm flux correspond to the obtained changes in planetary waves amplitudes. Changes in the conditions of propagation and reflection of stationary planetary waves caused by impacts of solar activity on the thermosphere can influence atmospheric circulation in a broad altitude range including the middle atmosphere.

1. Introduction

Large-scale wave disturbances in the atmosphere contribute to the energy transfer between different atmospheric layers and play significant role in the formation of the general circulation of the middle and upper atmosphere (Holton, 1975). According to Haynes et al. (1991), wave disturbances in the upper mesosphere and thermosphere are the most prominent driving force affecting the extratropical circulation. Due to the rapid development of computer technology and the improvement of numerical models of the atmospheric general circulation, interest in a more accurate study of the dynamical and thermal effects produced by wave motions, in particular, by planetary waves (PWs) at different atmospheric layers is constantly increasing. Numerical simulations of planetary waves having different periods and zonal wavenumbers were performed recently (e.g., Liu et al., 2004; Chang et al., 2014; Wang et al., 2017).

The incoming solar radiation and heating depend on the solar activity (SA), which undergoes cyclic changes with a period of about 11 years (see e.g., Hathaway, 2010). Changes in the SA can affect the temperature and circulation, changing the conditions for the propagation and reflection of PW in the upper atmosphere (Geller and Alpert, 1980; Arnold and Robinson, 1998). Chanin (2006) compared the measurements and numerical simulations over 45 years and showed that changes in the SA in

the upper atmosphere strongly affect the PW propagation conditions, which can redistribute the incoming solar energy. It was confirmed by Krivolutsky et al. (2015), who performed numerical simulations to investigate the effect of the cyclicity of the SA on the temperature and zonal wind in the altitude range from 0 to 135 km. An important role of PW, transporting the energy between the upper atmosphere and the underlying layers was shown. For example, remote temperature measurements at altitudes of the mesopause in 1980–2007 showed the presence of PW with periods of 2–10 days, correlating with the 22-year “Hale cycle” (Hoppner and Bittner, 2007). A positive correlation between the change in the solar flux and PW activity with periods of 3–20 days was observed in the analysis of long-term observations of wind at heights of the mesosphere-lower thermosphere (MLT) (Jacobi et al., 2008). Recently, Gan et al. (2017) investigated the annual-mean and seasonal variations of temperature response to the 11-year solar cycle in the mesosphere. They simulated the global circulation for 31 years and compared the results of simulation with the 14-year observation data obtained by broadband emission radiometry (TIMED/SABER). When analyzing Eliassen–Palm flux and gravity wave drag, they found that under the solar maximum conditions, the PW activity is weaker, leading to the westerly zonal wind anomaly in the upper winter stratosphere and lower mesosphere. PW reflection in the lower thermosphere may also influence the circulation of the middle atmosphere (e.g., Lu et al., 2017).

* Corresponding author.

E-mail addresses: a.v.koval@spbu.ru (A.V. Koval), apogor@rshu.ru (A.I. Pogoreltsev).

<https://doi.org/10.1016/j.jastp.2018.03.012>

Received 12 December 2017; Received in revised form 19 February 2018; Accepted 15 March 2018

Available online 16 March 2018

1364-6826/© 2018 Elsevier Ltd. All rights reserved.

One of the reasons for the PW reflection at the thermospheric heights can be significant temperature and wind gradients.

Most of the numerical models used to estimate the propagation and reflection of PWs in the thermosphere have their upper boundaries at altitudes of about 120–150 km. Pogoreltsev et al. (2007) developed a thermospheric version of the middle and upper atmosphere model (MUAM), which allows numerical simulating of the general circulation and PWs in the atmosphere at altitudes from the Earth's surface up to about 300 km. In recent years, different versions of the MUAM were used to study the dynamical and thermal effects of orographic gravity waves (OGW) on the general circulation of the middle and upper atmosphere (Gavrilov et al., 2013) and on the meridional circulation and ozone fluxes (Koval et al., 2015). In addition, the interaction between OGW and PW during sudden stratospheric warming events (Gavrilov et al., 2017) and under different phases of quasi-biennial oscillations of the near-equatorial zonal wind (Koval et al., 2016) were studied.

In this study, the MUAM was used to study the propagation and reflection of the stationary planetary waves (SPW) under changes in the thermosphere caused by high and low levels of the SA. To “isolate” the thermospheric influence, the SA changes were specified in the model only at the altitudes higher than 100 km. At the lower altitudes, in all simulations, identical conditions corresponding to the medium level of SA were used. This approach makes it possible not only to consider circulation changes in the thermosphere but also to estimate the thermospheric influence on the circulation and thermal regime of the middle atmosphere.

2. The numerical model and solar activity accounting

In order to investigate the effect of SA changes on the global circulation and characteristics of SPW, the numerical experiments with the MUAM model (Pogoreltsev, 2007; Pogoreltsev et al., 2007) were performed. The MUAM solves the standard set of hydrostatic equations in spherical coordinates. In the current version of the MUAM, the horizontal grid has 36 nodes in latitude and 64 nodes in longitude. The vertical grid has 56 levels covering the heights from the Earth's surface to about 300 km. The geopotential height of the upper boundary depends on the atmospheric temperature as far as the log-isobaric vertical coordinate is used in the model. The time step was set to 225s. At the lower boundary, the amplitudes of the SPW are set in the model according to geopotential height distributions in the lower atmosphere taken from the JRA-55 (Japanese 55-year Reanalysis) database (Kobayashi et al., 2015) for January averaged over the years 2005–2014. Koval et al. (2015) described in details the stages of initialization of the MUAM. The modeling starts from an initial windless state with the JRA-55 global averaged temperature profile for January. During the first 130 model days, the MUAM uses only the daily averaged heating rates. Then daily variations of the solar heating and additional prognostic equation for the geopotential height at the lower boundary are included. This prognostic equation needs to satisfy the lower boundary condition for the waves generated by the internal sources. Starting from 330th model day, seasonal changes in the solar heating are included, and the next 60 days are considered as characteristic for the January-February conditions. Changing the starting day of the daily variations of solar heating around 130th model day enforces changes in phases of stratospheric vacillations of the mean zonal wind and PW characteristics (Pogoreltsev, 2007). In order to create two 12-member ensembles of the MUAM simulations (for the high and low SA, respectively), the starting day for the diurnal variability of the solar heating and prognostic equation for the geopotential height was changed between 120th and 131th with step of 1 model day.

The radiative block of the MUAM takes into account the dependence of solar radiation on the SA. The main indicator of SA is the solar radio flux at the wavelength of 10.7 cm ($F_{10.7}$). The $F_{10.7}$ flux changes during the 11-year solar activity cycle (e.g., Tapping, 1987). Our analysis of $F_{10.7}$ observations during the last six solar cycles (Royal Observatory of

Belgium(ROB), 2013) leads to values of $F_{10.7}=70, 130, 220$ sfu ($1 \text{ sfu} = 10^{-22} \text{ W}/(\text{m}^2\text{Hz})$), which are taken here to characterize the low, medium and high SA levels, respectively. The main purpose of this study is to consider effects of SA changes occurring in the thermosphere only (see above). Therefore, different $F_{10.7}$ values in the radiative and thermospheric blocks of the MUAM were set only at altitudes above 100 km. Below 100 km, in all simulations, the constant value of $F_{10.7}=130$ sfu, corresponding to the medium SA level, was used.

To take into account the effects of ionospheric charged particles on the neutral gas motion, ionospheric conductivities with their latitudinal, longitudinal and temporal variability (Shevchuk et al., 2018) are taken into account in the MUAM. Geomagnetic torque and ion drag terms were determined, respectively, by the formulas (Shevchuk et al., 2018):

$$M = \frac{\sigma_2 H_z H_0}{c^2}; I = \frac{\sigma_1 H_0^2}{\rho c^2}, \quad (1)$$

where H_0, H_z are the module of the magnetic field intensity vector and its vertical component, respectively; c is the speed of light; ρ is the density of the neutral atmosphere; σ_1 and σ_2 are, respectively, the ionospheric Pedersen and Hall conductivities, calculated as follows (e.g., Pogoreltsev, 1996):

$$\sigma_1 = eN(\mu_1^e + \mu_1^i); \sigma_2 = eN(\mu_2^e - \mu_2^i) \quad (2)$$

Here e, N are the electron charge and the number electron density, respectively, $\mu_1^e, \mu_2^e, \mu_1^i, \mu_2^i$ are the preambilities of electrons and ions, respectively.

Geomagnetic torque and ion drag calculations were performed using equation (1) including ionospheric parameters taken from semi-empirical models of the neutral atmosphere: NRL-MSISE and ionosphere: IRI-Plas (Shevchuk et al., 2018). The values of the calculated geomagnetic torque and ion drag for January were implemented into the MUAM, taking into account diurnal variations at all latitudes, longitudes and 23 vertical levels above 100 km.

One of the input parameters for the NRL-MSISE and IRI-Plus models is the $F_{10.7}$ flux, which allows us to take into account the dependence of atmospheric and ionospheric characteristics on the variations of the SA by using $F_{10.7}=70$ sfu and $F_{10.7}=220$ sfu for low and high SA levels, respectively. Thus, the SA dependence of the modelled ionospheric conductivities in the MUAM is determined by the dependence of ionospheric parameters (electron concentration, composition of the neutral and ionized components, etc.) on $F_{10.7}$ flux.

To interpret the model calculations of SPW amplitudes, the latitude-altitude distributions of the mean-zonal quasi-geostrophic complex refractivity index (RI) squared were utilized, which was calculated as follows (e.g., Albers et al., 2013; Gavrilov et al., 2015):

$$n_m^2(\varphi, z) = \frac{\bar{q}_\varphi}{\bar{u} - c} - \left(\frac{m}{a \cos \varphi} \right)^2 - \left(\frac{f}{2NH} \right)^2, \quad (3)$$

where m is the zonal wavenumber; \bar{q}_φ is the latitudinal gradient of zonal-mean potential vorticity; \bar{u} is the zonal mean zonal wind speed; $c = 2\pi a \cos \varphi / (m\tau)$ is the zonal phase speed; τ is the wave period; φ and z are latitude and altitude; a is the Earth radius; f is the Coriolis parameter; N is the buoyancy frequency; H is the atmospheric pressure scale height. According to Dickinson (1968) and Matsuno (1970), PW propagate in regions of the atmosphere where $n_m^2(\varphi, z) > 0$ and damp at a negative n_m^2 values. Regions of the positive n_m^2 can be considered as the waveguides.

The second important PW characteristic, which we used in the present study for further diagnostics of SPW propagation, is the vertical component of the Eliassen-Palm flux (EP-flux) vector (Andrews et al., 1987). According to the theory, an upward direction of EP-flux vector relates to the northward wave heat flux, while downward EP-flux relates to the southward wave heat flux. The divergence of the EP-flux shows the net drag of the zonal-mean flow by the PWs.

3. Results of simulation

To account for the effects of the SA changes only in the thermosphere, a constant medium SA level was set in the MUAM at the altitudes below 100 km. Above 100 km level, SA was specified for the low to high levels (see section 2). To obtain statistically significant results, two 12-member ensembles with conditions corresponding to the high and low SA were calculated. Wind, temperature, and geopotential height fields were obtained and averaged over January-February and over the longitude circles to get zonal-mean characteristics for each model run. The longitude-time Fourier transform with the least squares fitting of the geopotential heights estimates the SPW amplitudes and phases. Besides improving statistical significance, averaging over two months and over 12 model runs allows us to avoid such extreme dynamical effects as SSW events occurring in separate runs. The impact of separate extreme events was “smoothed out” and could not influence global circulation and SPW propagation.

We analyzed the averaged over 12 model runs differences in the atmospheric general circulation and the amplitudes of the SPWs with zonal wavenumbers $m = 1-4$ (referred to as SPW1 – SPW4 hereinafter) caused by SA impacts on the thermosphere.

3.1. General circulation

Fig. 1a, b and c show, respectively, the altitude-latitude distributions of the zonal-mean wind, temperature and meridional temperature gradient averaged over January-February and 12 model runs for high and low SA along with differences between them. The general structure of the zonal circulation in Fig. 1a corresponds to empirical models (e.g., Jacobi et al., 2009). At the altitudes higher than 160-180 km, the zonal wind is significantly stronger (up to 50%) at a high SA in the left panel of Fig. 1a. Between 140 and 180 km in the Southern Hemisphere the zonal wind is stronger under the high SA (see positive wind differences in the right panel of Fig. 1a), which is connected with corresponding positive

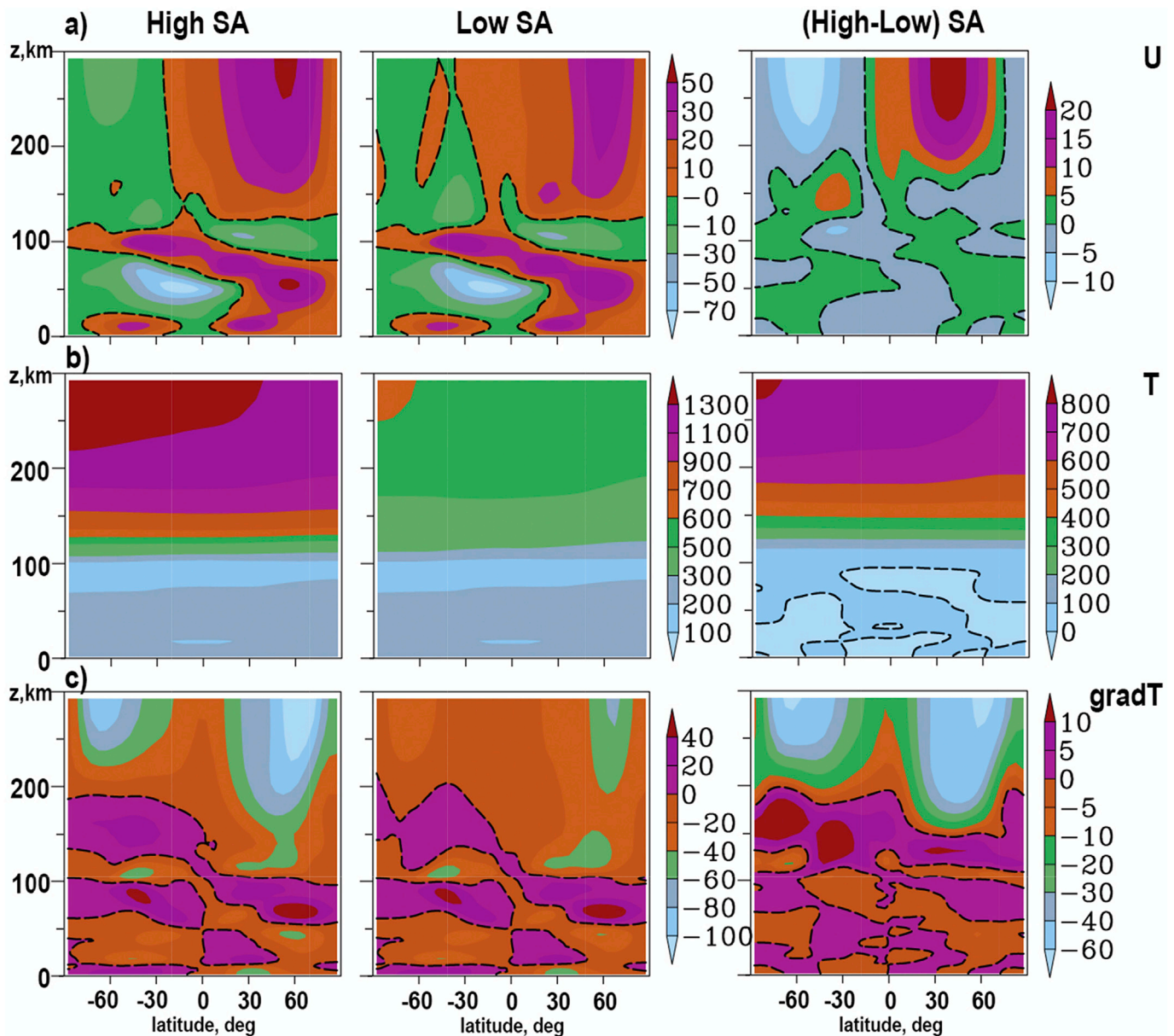


Fig. 1. High-latitude distributions of the averaged over January-February and 12 model runs zonal-mean zonal wind in m/s (a), temperature in K (b) and meridional temperature gradient in K/deg (c) at the high (left) and low (center) SA level along with and differences between the corresponding values (right). Dashed contours correspond to zero values.

differences of the meridional temperature gradient in the right panel of Fig. 1c. At altitudes below 100 km, there are minor differences in zonal wind in the right panel of Fig. 1a. For example, the zonal wind differences at middle latitudes of the Northern Hemisphere at altitudes 60–100 km may reach 3 m/s (about 6% of the corresponding peak values). This shows that modifications of thermospheric parameters caused by the SA change at altitudes above 100 km can influence the global circulation at the middle-atmospheric heights.

To estimate statistical significance of the differences in the right panels of Fig. 1, the standard Student's t-test was used. The differences in the right panels of Fig. 1 were calculated using $12 \times 720 \times 64 = 552960$ pairs of respective values for the low and high SA, obtained from 12 model runs, 720 time steps (2-h outputs) in 64 longitude grid nodes. Application of statistical paired Student's t-test (e.g. Rice, 2006) gives 99% statistical significance, if absolute values of the differences in the zonal mean zonal wind, temperature and in the meridional temperature gradient exceed 1 m/s, 1 K and 1 K/deg in the respective right panels of Fig. 1. Particularly, mentioned above differences in the zonal wind between the high and low SA at altitudes 30–80 km have enough statistical significance, when their absolute values exceed 1 m/s in the right panel of Fig. 1a.

The zonal wind velocity differences shown in the right panel of Fig. 1a can be explained by the influence of SA on the meridional temperature gradients in Fig. 1c. According to the theory, the thermal component of the zonal wind is proportional to the meridional temperature gradient. In the Northern Hemisphere, an increase in the meridional temperature gradient should correspond to a decrease in the zonal wind speed (e.g., Gill, 1982). A comparison of the right panels of Fig. 1a and c identifies that negative differences in the meridional temperature gradient in the Northern Hemisphere correspond usually to positive differences in the zonal velocity. In the Southern Hemisphere, the signs of differences in the meridional temperature gradient and the zonal velocity in the right panels of Fig. 1 are basically the same.

Consideration of the various heat influxes contributing to the MUAM equation for thermal balance shows that in the thermosphere solar heating is strongest at high latitudes of the Southern (summer) Hemisphere and it is weakest at high latitudes of the Northern (winter) Hemisphere (see Fig. 1b). Therefore, negative meridional temperature gradients dominate in Fig. 1c at altitudes above 180–200 km. Dynamical processes and atmospheric circulation produce additional heat influxes, among which the horizontal thermal advection and adiabatic temperature changes caused by vertical air movements predominate. These dynamical heat influxes could play an important role at altitudes of 100–200 km, where regions of positive temperature gradient appear in the Southern Hemisphere. Fig. 1c shows that at high SA level the meridional temperature gradients are smaller in the thermosphere at altitudes above 200 km and are larger at altitudes of 120–180 km. This explains respective changes in the mean zonal wind speed shown in Fig. 1a.

The SA effects on solar heat influx in our simulation are taken into account only at altitudes above 100 km. Therefore, the small differences (about 5% of the peak values) in the meridional temperature gradient and related differences in the zonal velocity seen in the respective right panels of Fig. 1a and c at altitudes below 100 km are caused by changes in thermospheric characteristics at altitudes above 100 km at different SA levels. Such changes in thermospheric parameters can produce changes in the propagation and reflection conditions of SPWs in the lower thermosphere due to SA changes, which are discussed in the next section.

3.2. SPW amplitudes and phases

The SPW amplitudes and phases are calculated using the longitude-time Fourier transform with the least squares fitting of the geopotential heights averaged over January-February and two 12-member ensembles (see section 2). Figs. 3 and 4 reflect distributions of the RI squared and vertical component of EP-flux, respectively. Comparisons of obtained

wave structures with satellite observations (Forbes and Zhang, 2002; Xiao et al., 2009; Mukhtarov et al., 2010) show that simulated SPW amplitudes are in agreement in magnitude and structure to the published ones.

Altitude-latitude distributions of SPW1-4 amplitudes are shown in Fig. 2a-d. Left and center panels correspond to high and low SA, respectively. Right plots reveal their differences. Fig. 3 represents respective phases of SPW: it shows longitudes of SPW maximum in degrees.

Corresponding to Figs. 2 and 3 refractivity, indices and EP-fluxes of SPW1-SPW4 are shown in Figs. 4 and 5, respectively.

The left and middle panels of Fig. 2 show that in the middle atmosphere the SPW amplitudes have the maxima at the middle and high latitudes of the Northern (winter) Hemisphere due to the eastward direction of the atmospheric circulation in the winter stratosphere-mesosphere. In the Southern (summer) Hemisphere, the zonal circulation is directed westward at altitudes 20–70 km in the left and middle panels of Fig. 1a, which can make difficulties for SPW propagation at these altitudes (e.g., Charney and Drazin, 1961). At altitudes above 100 km, significant SPW amplitudes exist in both hemispheres in the left and middle panels of Fig. 2. This is associated with wide SPW waveguides, where $n_m^2(\varphi, z) > 0$, which cross the equator in the mesosphere and span upwards in both hemispheres into the thermosphere in the left and middle panels of Fig. 4.

The left and center panels of Fig. 3a shows that sometimes differences in phases between the middle atmosphere and thermosphere can reach 180° , i.e. these waves oscillate in antiphase.

Areas inside dashed lines in the left and middle panels of Fig. 4 correspond to waveguides with positive n_m^2 values for respective SPW modes. Changes in the temperature and zonal velocity fields caused by the SA variations modify configurations of the SPW waveguides. Increasing zonal wavenumber m decreases the width of the waveguides in the thermosphere (see the left and middle panels in Fig. 4). Decrease of the SPW amplitudes in the thermosphere is also one of the reasons of the zonal wind enhancement at the corresponding layers. Negative in n_m^2 values and in the vertical component of EP-flux in the right panels of Figs. 4 and 5, respectively, may contribute to the degradation of SPW propagation conditions and to corresponding weakening of wave amplitudes in the right panels of Fig. 2 in respective regions of the thermosphere at the high SA level.

Regions shaded with lines in the right panels of Figs. 2–5 show places, where the paired Student's t-tests performed for the ensemble of 12 pairs of respective quantities at the high and low SA levels, gave smaller than 95% statistical confidence of nonzero differences between these quantities. The right panels of Fig. 2 show that at altitudes above 120–150 km in the most regions of the thermosphere, the SPW amplitudes are smaller under the high SA. According to the left and middle panels in Fig. 4, at the altitudes above 120 km the SPW waveguides are significantly narrower at the high SA than those at the low SA level. This is an important factor influencing the SPW propagation conditions.

In many cases, smaller negative differences of n_m^2 between the high and low SA levels in the thermosphere in the right panels of Fig. 4 correspond to negative differences in SPW amplitudes in the respective panels of Fig. 2. However, there are exceptions. For example, substantial positive differences in SPW1 amplitude at the high latitudes of the Northern thermosphere in the right panel of Fig. 2a is associated with corresponding negative n_m^2 differences in the right panel of Fig. 4a. The reason could be positive differences in the vertical EP-flux component in the right panel of Fig. 5a, which show stronger transfer of SPW1 activity to the thermosphere from below at the high SA level. For the SPW2 mode, one can see larger positive differences of the vertical EP-flux in the thermosphere at latitudes 30–60°N in the right panel of Fig. 5b. Negative differences in corresponding meridional EP-flux component indicate enhancement of southward EP-flux, which contributes to the larger transfer of the wave activity in the direction marked with the red arrow

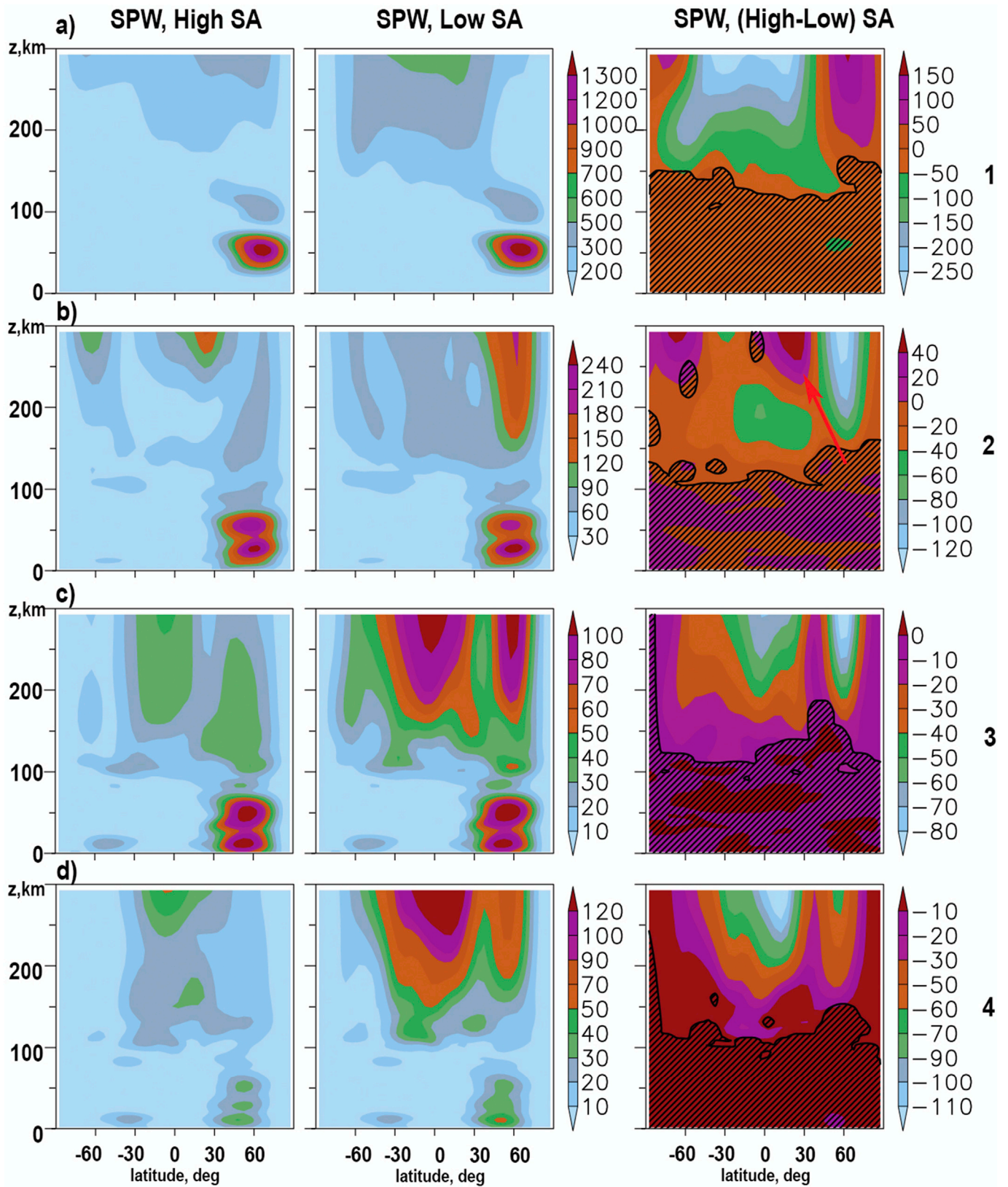


Fig. 2. Amplitudes of the geopotential height variations (in g.p.m.) caused by SPW1-SPW4 (a-d, respectively) under the high SA (left), low (center) SA, and their differences (right) for January-February, averaged over 12-members ensembles. Dashed contours correspond to zero values. Areas shaded with lines reflect statistically insignificant differences according to paired Student's t-test.

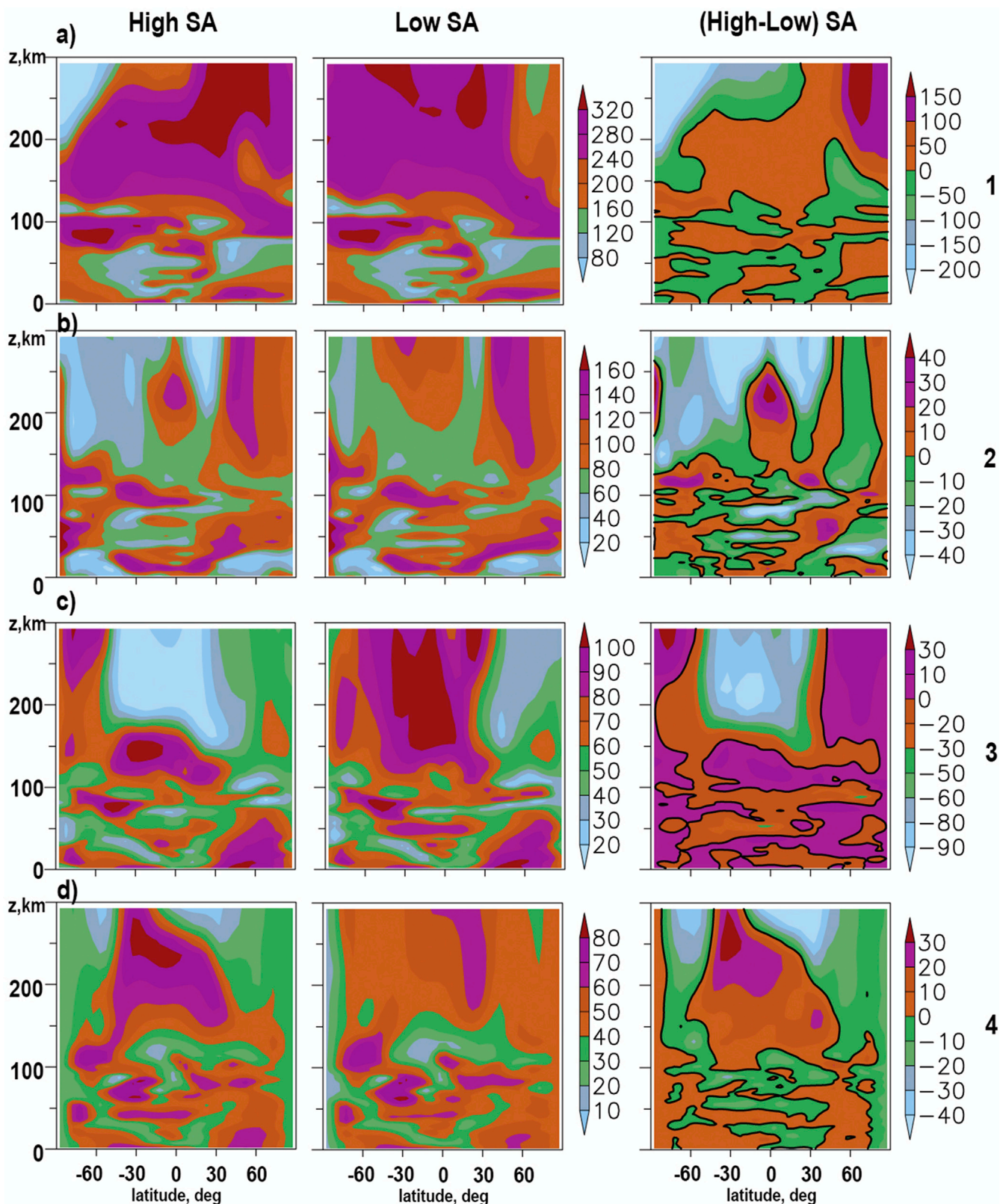


Fig. 3. The same as Fig. 2, but for the SPW phases (deg).

in the right panel of Fig. 2b. This can form larger SPW2 amplitudes in the near-equatorial upper thermosphere under the high SA. Similar mechanism may be also responsible for the positive differences in the SPW2 amplitude increase at altitudes above 250 km near the South Pole in the right panel of Fig. 2b.

In the thermosphere, the relative differences in SPW1 amplitudes between high and low SA can reach up to 30% in the right panel of Fig. 2a. Relative differences in SPW2 amplitudes in the thermosphere can reach 50% in the right panel of Fig. 2b. Positive differences in EP-flux and n_m^2 at high latitudes of the Southern thermosphere in the right panels of

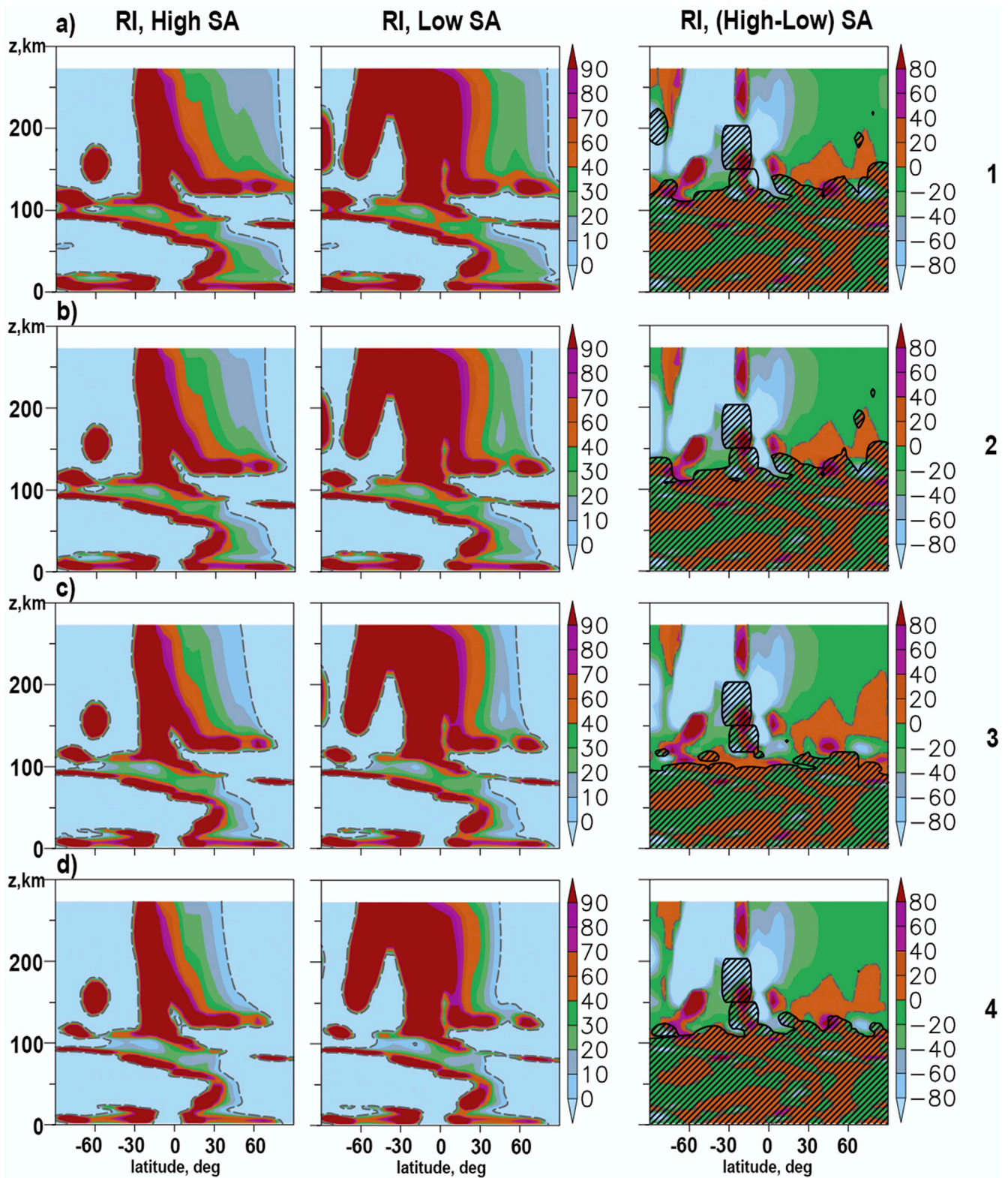


Fig. 4. The same as Fig. 2, but for the normalized $(a^2n_m^2)$ SPW refractivity index squared.

Fig. 4a and b and 5a,b generally correspond to larger SPW1 and SPW2 amplitudes at the high SA level in Fig. 2a and b.

The right panels of Fig. 2c and d shows smaller SPW3 and SPW4 amplitudes under high SA in the thermosphere, which correlate with negative n_m^2 differences in the respective panels of Fig. 4c and d. EP-flux differences in the right panels of Fig. 5a and b have smaller correlation

with SPW3 and SPW4 amplitudes behavior, however, the values of EP-flux differences could give less contribution to the SPW3 and SPW4 variability because of their relatively small values. Fig. 2c and d shows strong decreases (from 120 gpm to 50 gpm) in the SPW3 and SPW4 amplitudes in the low-latitude thermosphere due to change from the high to low SA.

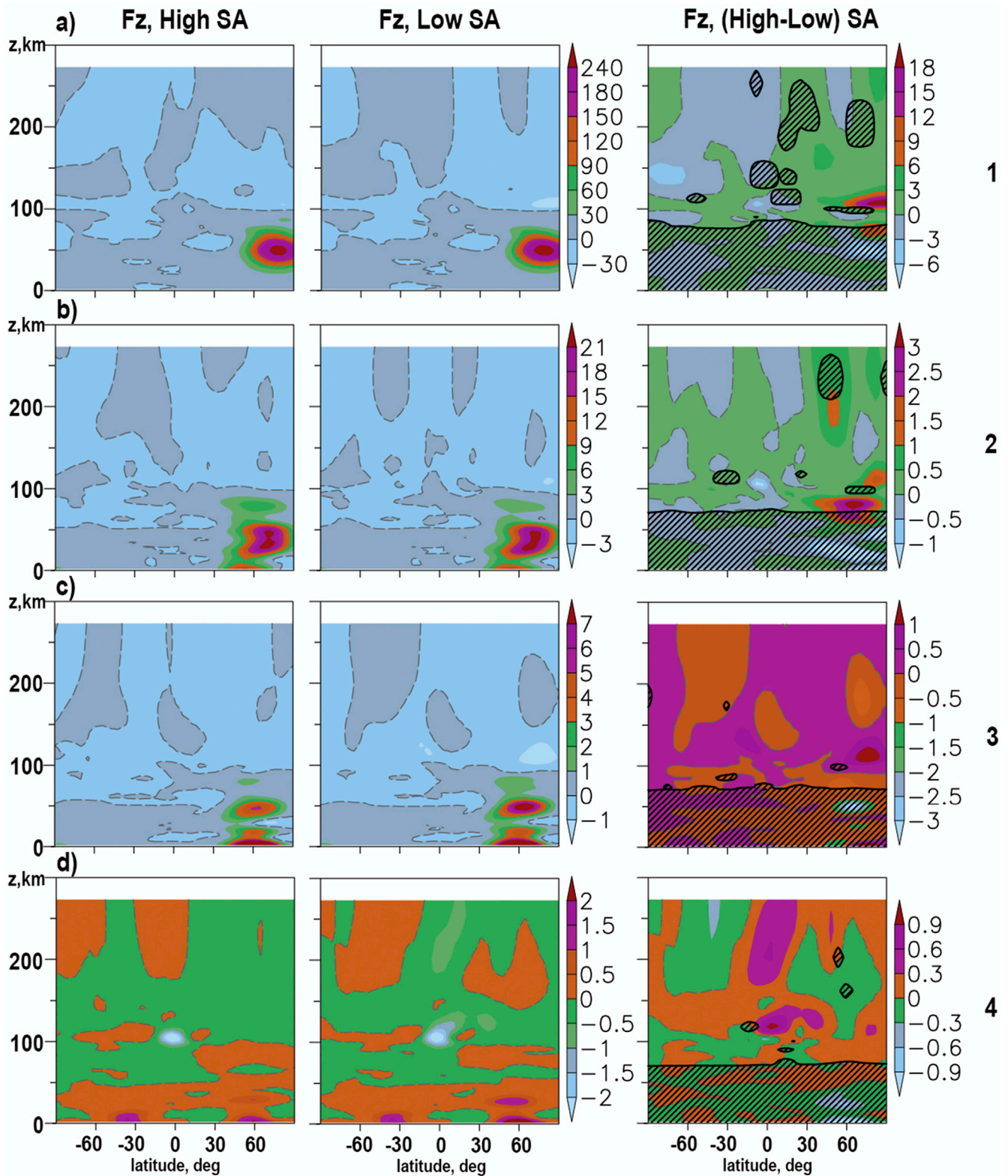


Fig. 5. The same as Fig. 2, but for the vertical component of the EP-flux vector in $10^{-2} \text{ m}^3/\text{s}^2$.

In Fig. 2, one can see substantial SPW amplitudes in the regions of the atmosphere located outside the respective waveguides shown in Fig. 4, where $n_m^2(\varphi, z) < 0$. In the most such cases, the EP-fluxes have nonzero values in these regions in Fig. 5. This can mean that the corresponding SPW modes can be generated in these regions inside the atmosphere, for example, due to the nonlinear wave-wave and wave-mean flow

interactions and/or nonzonal breaking of gravity waves.

In Fig. 2a below altitude of 100 km, one can see areas of small (up to 5%) differences in the SPW1 amplitude, which can be associated with changes in the strato-mesospheric SPW1 amplitude maxima in the Northern Hemisphere between the high and low SA. The differences in SPW2 amplitude at altitudes below 100 km can reach 10% in the right

panel of Fig. 2b. The statistical confidence of differences in SPW characteristics between the high and low SA conditions is smaller than 95% at altitudes below 100 km in Fig. 2. Therefore, much more model runs are required to obtain statistically reliable estimations of SPW amplitude differences caused by SA in the mesosphere and stratosphere. However, noticeable differences in the mean wind found above and having statistical confidants above 95% at altitudes below 100 km in the right panel of Fig. 1a may give evidences that modifications of thermospheric parameters could influence processes in the middle atmosphere.

A possible mechanism of thermospheric influences on the middle atmosphere dynamics could be changing conditions of the upward propagation of SPWs and a partial SPW reflection at high altitudes due to substantial increases (see Fig. 1b) in the thermospheric temperature at increasing solar activity (e.g., Arnold and Robinson, 1998; Lu et al., 2017). According to the PW theory (e.g., Andrews et al., 1987), the upward component of EP-flux corresponds to the northward SPW heat flux in the Northern Hemisphere, which can make warmer regions near the North Pole and, thus, influence the atmospheric circulation (e.g., Holton and Mass, 1976). Changes in the distributions of the vertical EP-flux component at all altitudes in Fig. 5 correspond to changes in n_m^2 in Fig. 4 influencing the SPW propagation conditions and to respective changes in wave amplitudes in Fig. 2 and the mean zonal wind in Fig. 1 at all altitudes, including the middle atmosphere.

Discussed above estimations with the statistical Student's t-test gave 99% statistical significance of nonzero differences of the mean zonal wind between the high and low SA, if the absolute values of the differences exceed 1 m/s in the right plot of Fig. 1a. This means adequate statistical confidence of peak zonal wind differences at altitudes 30–60 km reaching 3 m/s in Fig. 1a. However, the differences in SPW amplitudes, n_m^2 and vertical EP-flux at altitudes below 100 km lie in the areas shaded with lines in the right panels of Figs. 2–5, which correspond to less than 95% confidence of their nonzero values (see above). This shows that averaging over the 12-member ensembles of the MUAM simulations is not enough for adequate estimations of SPW parameter differences at high and low SA at altitudes below 100 km.

For a more detailed study of the SA effects below the thermosphere, more statistically reliable numerical modeling is desirable that takes into account not only thermospheric influence, but also effects of changes in solar irradiance and cosmic rays intensity on the thermal regime and dynamics of the middle atmosphere.

4. Conclusion

Using the thermospheric version of the MUAM numerical model, the 12-member ensembles of simulations of general circulation were obtained. The amplitudes of SPWs with the zonal wavenumbers $m = 1–4$ were calculated under high and low SA levels for January–February at altitudes from the Earth's surface up to 300 km. The SA changes are taken into account in calculations of solar heating and ionospheric conductivity at thermospheric heights above 100 km only. The influence of thermospheric SA effects on the SPW characteristics in the atmosphere was studied.

Numerical experiments have shown that changes in the thermal and dynamical regimes in the thermosphere with a changing SA can significantly affect the SPW propagation and reflection conditions in the thermosphere. At altitudes above 140 km, SPW amplitudes are generally larger under the high SA than those under the low SA. This can be explained by significant SA influences on meridional temperature gradients lead to the changes in the vertical profiles of the zonal wind, and the SPW propagation conditions. In the thermosphere, the relative differences in SPW1 amplitudes between high and low SA can be up to 30%. For SPW2, the differences in SPW2 amplitudes can reach 50%, and those for the SPW3 and SPW4 could be more than 50%. Values of the refractive index squared in the thermosphere are generally smaller and respective SPW waveguides are narrower at high SA level. At altitudes above 70–

80 km, SPWs can propagate along waveguides not only in the Northern, but also in the Southern Hemisphere, where the SPW amplitudes in the thermosphere are larger under the low SA level.

The SA effects at altitudes above 100 km can produce statistically significant changes in the mean zonal wind up to 3 m/s in the mid-latitude Northern Hemisphere at altitudes 30–100 km. They can be associated with corresponding differences in meridional temperature gradients as well as SPW amplitudes, refractive index and EP-fluxes. The statistical confidence of differences in SPW characteristics between the high and low SA conditions is smaller than 95% at altitudes below 100 km. More statistically reliable simulations are required, which could involve not only thermospheric influence, but also effects of changes in solar irradiance and cosmic rays intensity on the thermal regime and dynamics of the middle atmosphere.

Acknowledgments

The work was supported by the Grant Council of the President of the Russian Federation (grant MK-1424.2017.5).

References

- Albers, J.R., McCormack, J.P., Nathan, T.R., 2013. Stratospheric ozone and the morphology of the northern hemisphere planetary waveguide. *J. Geophys. Res. Atmos.* 118, 563–576. <https://doi.org/10.1029/2012JD017937>.
- Andrews, D.G., Holton, J.R., Leovy, C.B., 1987. *Middle Atmosphere Dynamics*. Acad. Press, New York, 489 pp.
- Arnold, N.F., Robinson, T.R., 1998. Solar cycle changes to planetary wave propagation and their influence on the middle atmosphere circulation. *Ann. Geophysicae* 16 (1), 69–76.
- Chang, L.C., Yue, L., Wang, W., Wu, Q., Meier, R.R., 2014. Quasi two day wave-related variability in the background dynamics and composition of the mesosphere/thermosphere and the ionosphere. *J. Geophys. Res.: Space Physics* 119 (6), 4786–4804.
- Chanin, M.-L., 2006. Signature of the 11-year cycle in the upper atmosphere. *Space Sci. Rev.* 125, 261–272. <https://doi.org/10.1007/s11214-006-9062-5>.
- Charney, J.G., Drazin, P.G., 1961. Propagation of planetary-scale disturbances from the lower into the upper atmosphere. *J. Geophys. Res.* 66, 83–109.
- Dickinson, R.E., 1968. Planetary Rossby waves propagating vertically through weak westerly wave guides. *J. Atmos. Sci.* 25, 984–1002.
- Forbes, J.M., Zhang, X., 2002. Climatological features of mesosphere and lower thermosphere stationary planetary waves within ± 40 latitude. *J. Geophys. Res.* 107 (D17), 4322. <https://doi.org/10.1029/2001JD001232>.
- Gan, Q., Du, J., Fomichev, V.I., Ward, W.E., Beagley, S.R., Zhang, S., Yue, J., 2017. Temperature responses to the 11 year solar cycle in the mesosphere from the 31 year (1979–2010) extended Canadian Middle Atmosphere Model simulations and a comparison with the 14 year (2002–2015) TIMED/SABER observations. *J. Geophys. Res.: Space Phys.* 122 (4), 4801–4818.
- Gavrilov, N.M., Koval, A.V., Pogoreltsev, A.I., Savenkova, E.N., 2013. Numerical simulation of the response of general circulation of the middle atmosphere to spatial inhomogeneities of orographic waves. *Izvestiya - Atmospheric and Ocean Physics* 49 (4), 367–374.
- Gavrilov, N.M., Koval, A.V., Pogoreltsev, A.I., Savenkova, E.N., 2015. Simulating influences of QBO phases and orographic gravity wave forcing on planetary waves in the middle atmosphere. *Earth Planets Space* 67, 86. <https://doi.org/10.1186/s40623-015-0259-2>.
- Gavrilov, N.M., Koval, A.V., Pogoreltsev, A.I., Savenkova, E.N., 2017. Simulating planetary wave propagation to the upper atmosphere during stratospheric warming events at different mountain wave scenarios. *Advances in Space Research*. <https://doi.org/10.1016/j.asr.2017.08.022>.
- Geller, M.A., Alpert, J.C., 1980. Planetary wave coupling between the troposphere and the middle atmosphere as a possible Sun-weather mechanism. *J. Atmos. Sci.* 37, 1197–1215.
- Gill, A.E., 1982. *Atmosphere-ocean Dynamics*. Academic Press, 662 pp.
- Hathaway, D.H., 2010. The solar cycle. *Living Rev. Solar Phys.* 7, 1.
- Haynes, P.H., McIntyre, M.E., Shepherd, T.G., Marks, C.J., Shine, K.P., 1991. On the “downward control” of extratropical diabatic circulations by eddy-induced mean zonal forces. *J. Atmos. Sci.* 48 (4), 651–678.
- Holton, J.R., 1975. *The dynamic meteorology of the stratosphere and mesosphere*. Meteorol. Monogr. 15 (37), 218 pp.
- Holton, J.R., Mass, C., 1976. Stratospheric vacillation cycles. *J. Atmos. Sci.* 33, 2218–2215.
- Hoppner, K., Bittner, M., 2007. Evidence for solar signals in the mesopause temperature variability? *J. Atmos. Solar-Terr. Phys.* 69, 431–448.
- Jacobi, Ch., Fröhlich, K., Portnyagin, Y., 2009. Semi-empirical model of middle atmosphere wind from the ground to the lower thermosphere. *Adv. Space Res.* 43, 239–246.
- Jacobi, Ch., Hoffmann, P., Kurschner, D., 2008. Trends in MLT region winds and planetary waves, Collm (52°N, 15°E). *Ann. Geophysicae* 26 (5), 1221–1232.

- Kobayashi, S., Ota, Y., Harada, H., 2015. The JRA-55 Reanalysis: general specifications and basic characteristics. *J. Meteorol. Soc. Jpn.* 93, 5–48. <https://doi.org/10.2151/jmsj.2015-00>.
- Koval, A.V., Gavrilov, N.M., Pogoreltsev, A.I., Savenkova, E.N., 2015. Experiments on sensitivity of meridional circulation and ozone flux to parameterizations of orographic gravity waves and QBO phases in a general circulation model of the middle atmosphere. *Geosci. Model Dev. Discussions* 8 (7), 5643–5670. <https://doi.org/10.5194/gmdd-8-5643-2015>.
- Koval, A.V., Gavrilov, N.M., Pogoreltsev, A.I., Savenkova, E.N., 2016. Comparisons of planetary wave propagation to the upper atmosphere during stratospheric warming events at different QBO phases. *J. Atmos. Solar-Terr. Phys.* <https://doi.org/10.1016/j.jastp.2017.04.013>.
- Krivolutsky, A.A., Cherepanova, L.A., Dement'eva, A.V., Repnev, A.I., Klyuchnikova, A.V., 2015. Global circulation of the Earth's atmosphere at altitudes from 0 to 135 Km simulated with the ARM model. Consideration of the solar activity contribution. *Geomagn. Aeron.* 55 (6), 780–800.
- Liu, H.L., Talaat, E.R., Roble, R.G., Lieberman, R.S., Riggins, D.M., Yee, J.H., 2004. The 6.5-day wave and its seasonal variability in the middle and upper atmosphere. *Journal of Geophysical Research-Atmospheres* 109 (D21). <https://doi.org/10.1029/2004jd004795>.
- Lu, H., Scaife, A.A., Marshall, G.J., Turner, J., Gray, L.J., 2017. Downward wave reflection as a mechanism for the stratosphere-troposphere response to the 11-year solar cycle. *J. Clim.* 30 (N), 2395–2414. <https://doi.org/10.1175/JCLI-D-16-0400.1>.
- Matsuno, T., 1970. Vertical propagation of stationary planetary waves in the winter Northern Hemisphere. *J. Atmos. Sci.* 27 (6), 871–883.
- Mukhtarov, P., Pancheva, D., Andonov, B., 2010. Climatology of the stationary planetary waves seen in the SABER/TIMED temperatures (2002–2007). *J. Geophys. Res.* 115, A06315. <https://doi.org/10.1029/2009JA015156>.
- Pogoreltsev, A.I., 1996. Production of electromagnetic field disturbances due to the interaction between acoustic gravity waves and the ionospheric plasma. *J. Atmos. Terr. Phys.* 58 (10), 1125–1141.
- Pogoreltsev, A.I., 2007. Generation of normal atmospheric modes by stratospheric vacillations. *Izvestiya Atmos. Ocean. Phys.* 43 (4), 423–435.
- Pogoreltsev, A.I., Vlasov, A.A., Froehlich, K., Jacobi, Ch., 2007. Planetary waves in coupling the lower and upper atmosphere. *J. Atmos. Solar-Terr. Phys.* 69, 2083–2101. <https://doi.org/10.1016/j.jastp.2007.05.014>.
- Rice, J.A., 2006. *Mathematical Statistics and Data Analysis*, third ed. Duxbury Press, Pacific Grove. 603 pp. ISBN-10: 0534399428.
- Sunspot Index and Long-term Solar Observations database, Royal Observatory of Belgium (ROB). <http://sidc.be/silso/datafiles>.
- Shevchuk, N.O., Ortikov, m.Yu., Pogoreltsev, A.I., 2018. Simulation of atmospheric tides taking into account the diurnal variability of ionospheric conductivities. *Russ. J. Phys. Chem. B* 12 in press.
- Tapping, K.F., 1987. Recent solar radio astronomy at centimeter wavelength: the temporal variability of the 10.7-cm flux. *J. Geophys. Res.* 92 (D1), 829–838.
- Wang, J.C., Chang, L.C., Yue, J., Wang, W., Siskind, D.E., 2017. The quasi 2 day wave response in TIME-GCM nudged with NOGAPS-ALPHA. *J. Geophys. Res.: Space Physics* 122 (5), 5709–5732.
- Xiao, C., Xiong Hu, X., Tian, J., 2009. Global temperature stationary planetary waves extending from 20 to 120 km observed by TIMED/SABER. *J. Geophys. Res.* 114, D17101. <https://doi.org/10.1029/2008JD011349>.